



Fuel cell technology: Synthesis and electrical properties of electrolyte for intermediate temperature

A. El Himri^{1*}, K. Haboubi¹, M. El Himri², F. Dimane¹, F. Jeffali⁴, I. Hanafi¹, P. Núñez³

¹Laboratory of Engineering Sciences and Applications, National School of Applied Sciences, University of Mohammed Premier, Al Hoceima, Morocco

²Laboratory of Analytic and Molecular Chemistry, Polydisciplinary Faculty, University of Cadi Ayyad, Safi, Morocco

³Department of Inorganic Chemistry, University of La Laguna, Tenerife, Spain

⁴Laboratoire de Dynamique et d'Optique des Matériaux, Faculté des Sciences, Université Mohamed Premier, Oujda, Morocco

Received 05 May 2016, Revised 24 Jul 2016, Accepted 01 Aug 2016

*Corresponding author, E-mail: name2004@hotmail.com,

Abstract

Ce_{0.9}Gd_{0.1}O_{2-δ} fine powder has been synthesized by a simple and fast hydrothermal method at relatively low temperature (140 °C) from high-purity commercial CeO₂ and Gd₂O₃. The X ray diffraction results showed that the crystalline powder is single phase with cubic fluorite structure; the average crystallite size was about 8.6 nm. The electrolyte pellets sintered at 1100-1300 °C were dense, with relative densities over 96%. Impedance spectroscopy was used to analyze the electrical transport properties between 150-1000 °C, with a systematic deconvolution of bulk and grain boundary properties in the lower temperature range. The results evidenced an improvement of the total conductivity in the low-temperature regime for sample sintered at 1100 °C, which was ascribed to an enhancement of the grain boundary properties. The implementation of the space charge layer model was used to identify modifications of the space charge potential with the sintering temperature.

Keywords: Hydrothermal synthesis; Sintering temperature; Impedance Spectroscopy; Ionic Conductivity; Grain boundary; Nanopowder.

1. Introduction

Fuel cell technologies have experienced a growing interest in the last few years as means to generate energy more efficiently than the combustion of fossil fuel. Thus, fuel cells are expected to substantially reduce oil dependency and environment impact [1-3]. Solid oxide fuel cells (SOFCs) are solid devices that produce electricity from the electrochemical combination of a hydrogen containing fuel and an oxidant such as oxygen or simply air [4]. Each single cell comprises two electrodes, an anode and a cathode, separated by an electrolyte.

The electrolyte for SOFCs must be stable in both reducing and oxidising environment, and must have sufficiently high ionic with negligible electronic conductivity at the operating temperature. Until now, standard electrolyte materials based on stabilised zirconia, especially yttria stabilised zirconia (YSZ), has been the most favored electrolyte [5], which requires operating temperature around 1000 °C to ensure sufficient ionic conductivity. However, reducing the operating temperature allows the use of cheaper construction materials and more reliable seals. Thus, an increasing attention is focused in lowering the operating temperature to 500-700 °C, which includes the study of electrolyte materials with higher ionic conductivity [6, 7].

Ceria-based solid electrolyte exhibits high ionic conductivity at intermediate temperature (600–800 °C), which is comparable with that of YSZ at high temperature [8-11]. The ionic conductivity can significantly be

improved by increasing the oxygen vacancies upon the substitution of a lower-valent metal ion as lanthanide dopants (e.g. gadolinium, samarium) [12-15].

Several divalent alkaline-earth and trivalent rare-earth oxides form extensive solid solution with ceria. Rare-earth doped ceria has been found [10] to be a more promising candidate as a solid electrolyte in SOFC which can be operated at intermediate temperature [16, 17]. Gadolinium-doped ceria (GDC) is considered to be one of the best ceria-based solid electrolytes because the cationic radius of Gd^{3+} is suggested to minimize defect interactions between the trivalent dopant and the oxygen vacancies [18-20].

Generally, ceramic materials are synthesised by solid state reaction: the powders are mixed, milled and annealed. Since the limited diffusion of reactants, the reaction requires high temperature ($T > 1200\text{ }^{\circ}\text{C}$), long heating period and intermediate milling to achieve good homogeneity. Other disadvantages of the method are the formation of undesirable phases, large grain sizes (low densification and surface area of materials) due to firing at high temperature and poor chemical homogeneity. A common feature of the new synthesis methodologies is their search for alternative reaction path through which the cationic diffusion distances are reduced and the precursor possesses high reactivity which allows a reduction in the temperature and/or sintering time [21-23].

Moreover, wet chemical processes provide a potential method for preparing materials with excellent control over purity, particle morphology and doping ratio at lower temperature [24, 25]. It is well known that the preparative route plays a critical role in governing materials properties, controlling the structure, morphology, grain size and surface area of the obtained materials.

In this work, we report a simple method for the synthesis of gadolinium doped ceria, $Ce_{0.9}Gd_{0.1}O_{2.8}$. A hydrothermal method was used to obtain homogeneous nanocrystalline precursors by a thermal decomposition process of precipitated gel of cerium and gadolinium oxides under low temperature calcination conditions. High-densified samples were obtained for sintering temperatures as low as 1100-1300 $^{\circ}\text{C}$, with important impact on the transport properties of the grain boundaries.

2. Experimental

2.1. Synthesis

Polycrystalline material with composition $Ce_{0.9}Gd_{0.1}O_{2.8}$ was prepared by the hydrothermal method. The appropriate quantities of CeO_2 (99.99%, Aldrich) and Gd_2O_3 (99.99%, Aldrich) were dissolved separately in nitric acid, mixed, and coprecipitated with concentrate ammoniac at pH 10. The precipitated gel and 2/3 of deionised water were sealed into Teflon-lined steel hydrothermal bomb and treated at 140 $^{\circ}\text{C}$ for several hours with a heating rate fixed at 10 $^{\circ}\text{C}/\text{min}$. The hydrothermal bomb was cooled to room temperature naturally. The resulting precipitate powder was repeatedly washed with deionised water and absolute ethanol, filtered, dried and characterized by X-ray diffraction.

2.2. Characterization

2.2. Materials characterisation

X-ray powder diffraction patterns were acquired using a Philips X'Pert Pro diffractometer, equipped with a Ge(111) primary monochromator and an X'Celerator detector. Routine pattern for phase identification was collected with a scanning step of 0.08° over the angular 2θ range $20-80^{\circ}$ with a collection time of 5 s per step. The graphical representation and structural analysis concerning XRD patterns were performed using WinPlotr and Fullprof programs [26].

The sinterability of the compound was evaluated by the linear shrinking behaviour of a green pellet from RT to 1150 $^{\circ}\text{C}$ at a heating rate of 5 $^{\circ}\text{C}/\text{min}$, using a thermomechanical analyser (Perkin Elmer TMA, Pyris Diamond).

2.3. Electrical measurements

Starting hydrothermal powders were uniaxially pressed into disks of 7 mm of diameter at 130 MPa. Dense pellets with relative density higher than 96% were obtained after sintered at 1100-1300 $^{\circ}\text{C}$ for 10 h. Pellets with thickness ~ 1 mm and diameter ~ 5 mm were fixed in an electrochemical setup of alumina with Pt-wires for the

electrical connections and then inserted into a quartz flow-through tube furnace. To ensure electrochemical reactions at the electrodes and good electrical contact between the platinum wires and the samples, each side of the pellet was painted with platinum paste and baked at 900 °C for 10 h.

Solartron 1260 impedance analyser was used for electrical characterisation, including an assessment of grain boundary effects. Impedance Spectra were obtained in the frequency range from 0.1 Hz to 1 MHz with an applied voltage of 25 mV in the temperature range of 500-1000 °C and 100 mV in the range 200-500 °C. Experimental measurements were controlled by the ZPlot program. Data analysis was made by equivalent circuits using the ZView program [27] allowing us to estimate the different contributions of the conductivity.

3. Results and discussion

3.1. Powder characterisation and densification

An XRD pattern of powder obtained directly from the hydrothermal process at 140 °C is shown in **Figure 1a**, where the peaks of $\text{Ce}_{0.9}\text{Gd}_{0.1}\text{O}_{2-\delta}$ fluorite single phase are exhibited. The peaks are relatively broad, which indicates that the crystallites are very small. The average size of the crystallites of gadolinium substituted ceria powder, calculated from the XRD pattern (by the standard Scherrer analysis of the half-width of the XRD peak, following the method described in ref. [28]), was 8.6 nm. Well crystallized LaB6 was used as standard to calibrate the intrinsic width associated to the equipment. A qualitative analysis of the XRD data indicated that the sample exhibited a single cubic phase (fluorite type-structure with space group Fm-3m) with a cell parameter of 5.4214 Å.

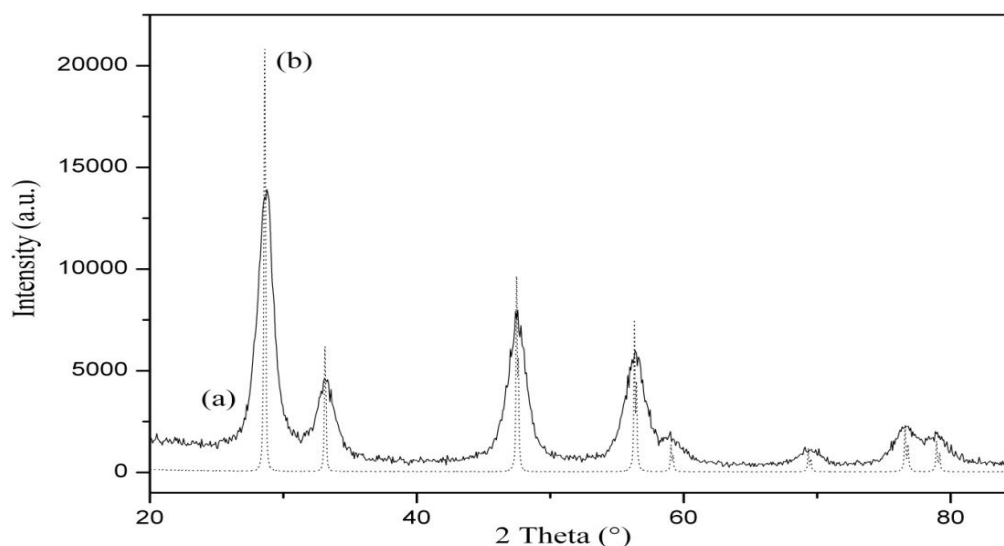


Figure 1. XRD pattern of $\text{Ce}_{0.9}\text{Gd}_{0.1}\text{O}_{2-\delta}$ powder resulting from hydrothermal synthesis at 140 °C (a) and the sample sintered at 1100 °C (b)

Figure 2 shows the linear shrinkage of the starting hydrothermal powder as a function of temperature. The densification process is located in a short range of temperature, starting around 400 °C and reaching the shrinkage rate peak at 720 °C. Above 1100 °C, only a minor densification is apparent, which is probably affected by the dynamic process during the characterisation.

The ultrafine doped ceria powder was sintered into pellets at different temperatures (1100, 1200 and 1300 °C) for 10 h. It is evident from **Figure 1b**, that the single cubic phase (Fm-3m) was preserved with an increase in grain size and crystallinity. The relative densities of $\text{Ce}_{0.9}\text{Gd}_{0.1}\text{O}_{2-\delta}$ electrolytes are listed in **Table 1** which depicts that sintered $\text{Ce}_{0.9}\text{Gd}_{0.1}\text{O}_{2-\delta}$ samples were over 96%. The powder synthesized by hydrothermal process can significantly decrease the sintering temperature, compared to that of ~ 1400 °C required for ceria solid electrolytes prepared by the classical solid state reaction.

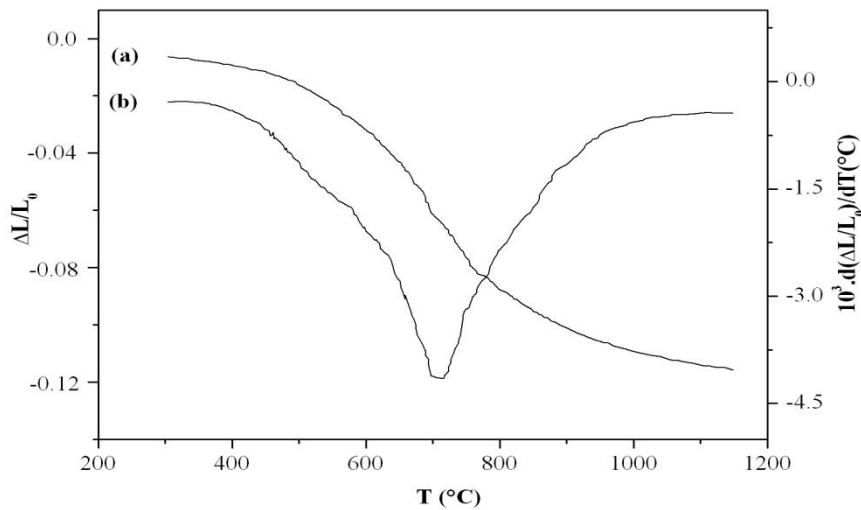


Figure 2. Linear shrinkage (a) and linear shrinkage rate (b) as a function of temperature of $\text{Ce}_{0.9}\text{Gd}_{0.1}\text{O}_{2-\delta}$ sample

This is an advantage to prepare polycrystalline materials with fine grain sizes, which can contribute to improve the physicochemical properties of the SOFC electrolytes. Low temperature synthesis methods give rise to materials with lower grain size and better reactivity and therefore could compromise the SOFC performance than those obtained by conventional solid state reaction. In addition, a more homogeneous density is obtained, which generally results in a high ionic conductivity and mechanical stability.

3.2. Electrical properties

Impedance spectroscopy has been widely used for the analysis of the electrical properties of solid-electrolyte materials due to the advantage of deconvolution between intragrain, intergrain and electrode/electrolyte interface contributions in a specific range of measuring temperature. The impedance spectra were fitted to the conventional equivalent circuit, containing three Resistance-Constant Phase Element (R-CPE) subcircuits in series, to take into account the three successive semicircles which can normally be resolved at low temperatures in the Nyquist plots (**Figure 3**).

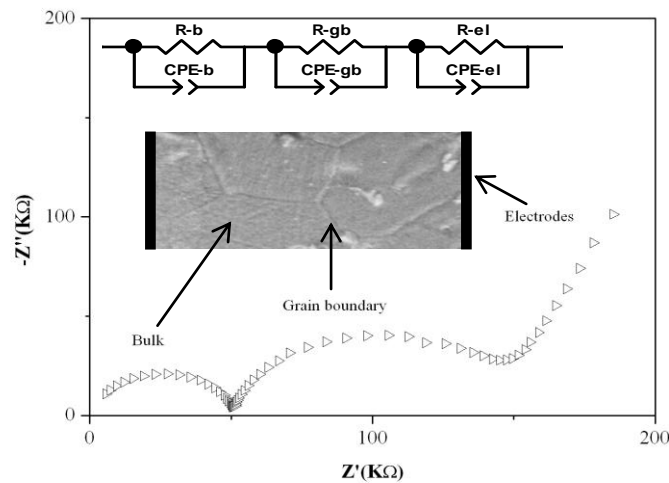


Figure 3. Typical impedance spectra obtained at 250 °C for $\text{Ce}_{0.9}\text{Gd}_{0.1}\text{O}_{2-\delta}$ sintered at 1100 °C.

Figure 4 shows the Arrhenius-type representation of total conductivity derived from the impedance spectra collected in air between 150-1000 °C for samples sintered at 1100, 1200 and 1300 °C for 10 hours.

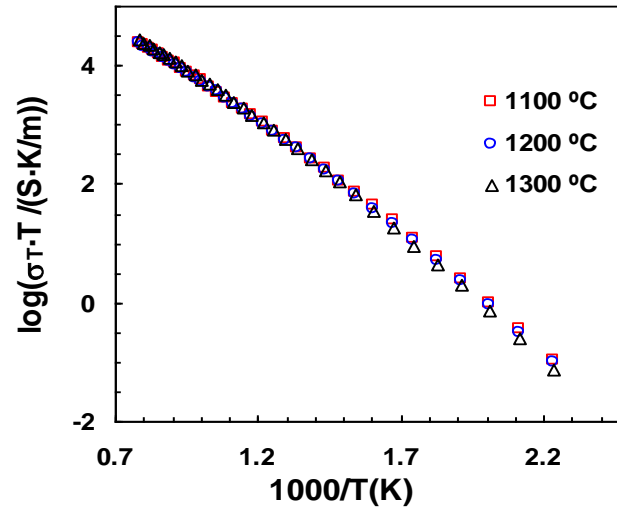


Figure 4. Arrhenius plot of total conductivities for $\text{Ce}_{0.9}\text{Gd}_{0.1}\text{O}_{2.6}$ samples sintered at different temperatures.

Table 1 Total conductivity and relative density of $\text{Ce}_{0.90}\text{Gd}_{0.10}\text{O}_{2.6}$ samples

Sintering temperature (°C)	Relative density (%)	Total conductivity, σ_T (Sm^{-1})				
		T_{test} (°C)				
		400	500	600	650	700
1100	96.22	0.17	0.73	2.13	3.03	4.32
1200	96.40	0.16	0.70	2.07	3.12	4.51
1300	96.78	0.15	0.69	2.03	3.19	4.63

As a consequence, the high-temperature-dependence of conductivity should be mainly influenced by the bulk properties, thus decreasing the activation energy of the overall electrical transport. Moreover, interaction between trivalent dopant (Gd^{3+}) and oxygen vacancies becomes more severe in the lower range of temperature, promoting also the increase of the activation energy [32-34].

In the low temperature range (150-400 °C), the conductivity is slightly higher for the samples sintered at lower temperatures and the values converge in the high temperature range for all the samples.

The situation is clarified by plotting the Arrhenius-type representation of bulk and grain boundary conductivities separately. The bulk and grain boundary conductivities of the samples were measured across a temperature range of 150 to 400 °C. At higher temperatures, the higher relaxation frequencies derived from the lower resistances of the samples hinder to resolve the semicircles corresponding to the bulk conductivity. However, the bulk resistance in the higher range of temperature ($R_{B,HT}$) can be estimated by the actual values of total resistance (R_T) and the linearly-extrapolated grain boundary resistance ($R_{gb,ext}$) according to [35]:

$$R_{B,HT} = R_T - R_{gb,ext} \quad (1)$$

Figure 5 shows that the bulk conductivity in the whole range of temperature is essentially independent of the sintering conditions. This indicates that no significant change in composition or phase of the bulk material was caused by sintering temperature. However, a bending is clearly appreciable as a function of the measuring temperature with activation energies decreasing from 0.72-0.74 eV to 0.56-0.58 eV, when moving from the lower to the higher regimes of temperature. This is a confirmation that the interaction between different charged species is more severe at lower temperature, suggesting that the bulk conductivity is affected by the association of defects ($\text{Gd}'_{\text{Ce}} \cdot \text{V}_{\text{O}}''$). Under the assumption that these defects are completely dissociated in the high-

temperature regime [11], the results suggest values of enthalpy for defect association of about ~0.16 eV, which agrees very well with the values of ~0.13-0.19 eV previously reported for Gd-doped ceria with 10% Gd [36].

It is important to emphasize that the Ce_{0.9}Gd_{0.1}O_{2-δ} electrolyte prepared by hydrothermal process and sintered at 1100 °C has a value of conductivity of about 3.03x10⁻² S.cm⁻¹ at 650 °C, which is close to the expected bulk conductivity of 3.20x10⁻² S.cm⁻¹, calculated by means of Eq. 1. This result suggests the low influence of the grain boundary resistance at intermediate temperature.

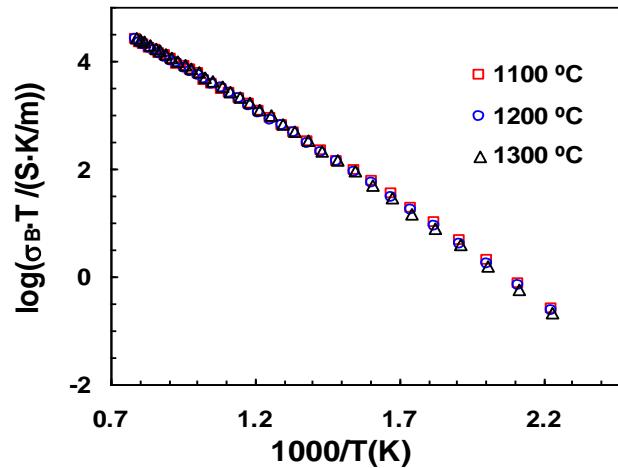


Figure 5. Arrhenius plot of bulk conductivity of Ce_{0.9}Gd_{0.1}O_{2-δ} sample sintered at different temperatures.

According to the brick-layer model [37], the experimental resistance related to transport across the grain boundaries (R_{gb}) is not only influenced by the grain boundary conductivity but also by the grain size and the grain boundary thickness, according to:

$$R_{gb} \frac{A}{L} = \frac{1}{\sigma_{gb}} \frac{\delta_{gb}}{d_g} \quad (2)$$

where σ_{gb} is the grain boundary conductivity, δ_{gb} is the average value of grain boundary thickness and d_g is the averaged grain size. As a general feature, a higher grain size is expected to contribute to decrease the grain boundary resistance. In contrast, the experimental grain boundary capacitance (C_{gb}) is expected to rise according to:

$$C_{gb} \frac{L}{A} = \epsilon_0 \epsilon_{r,gb} \frac{d_g}{\delta_{gb}} \quad (3)$$

where ϵ_0 is the permittivity of free space and $\epsilon_{r,gb}$ the relative permittivity of the grain boundary. **Figure 6** confirms higher values of normalized grain boundary capacitances for samples sintered at higher temperatures. These results are followed by higher values of normalized grain boundary resistance (**Figure 7**), in an opposite way to the simple brick layer model. This suggests modification of the specific transport properties with sintering conditions.

An Arrhenius plot of the grain boundary conductivity of the different samples is shown in **Figure 8**. This representation is based on the results of “specific” grain boundary conductivity, which accounts for the “true” transport properties of grain boundaries, given that it is independent of the microstructural parameters as grain size and grain boundary thickness. The specific grain boundary conductivity can be determined by recombination of Eqs. 2-3:

$$\sigma_{gb} = \frac{\epsilon_0 \epsilon_r}{R_{gb} C_{gb}} \quad (4)$$

where ϵ_r is the relative permittivity of the bulk.

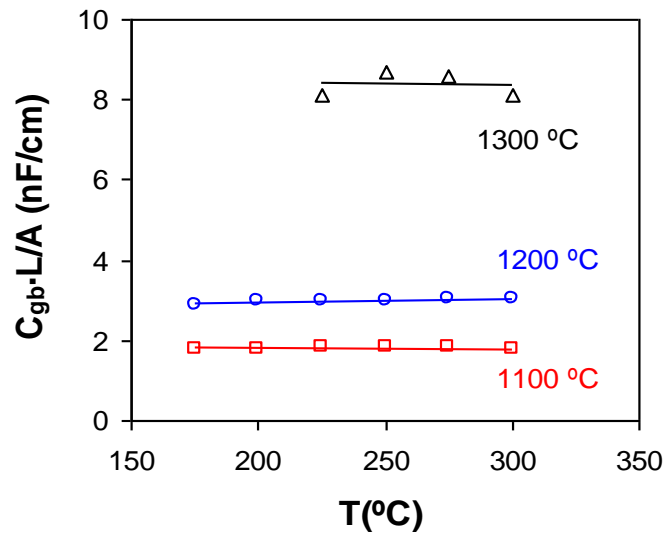


Figure 6. Geometrically normalized grain boundary capacitance for samples sintered at 1100-1300 °C.

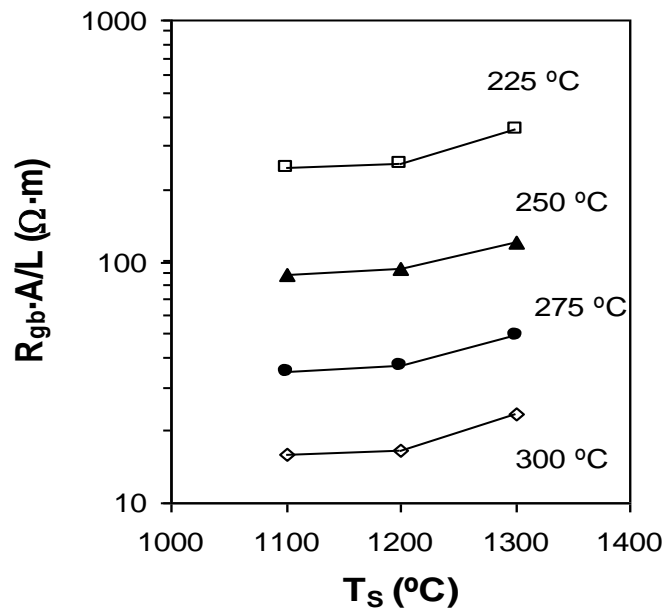


Figure 7. Geometrically normalized grain boundary resistance as a function of sintering temperature.

This expression is developed under the assumption that the permittivity of the grain boundary is close to that of the bulk, based on the findings that this parameter is insensitive to the dopant concentration in ceria-based materials [38]. However, the experimental values of bulk capacitances usually fail for determination of the bulk permittivity in samples with low values of A/L, as they may be obscured by the capacitive effects imposed by the experimental setup [39]. Therefore, the value of $\epsilon_r = 30$ obtained for samples with very high geometrical factor A/L [29] has been considered for determination of specific grain boundary conductivity according to Eq. 4.

It is apparent in **Figure 8** that across the entire range of temperature, the specific grain boundary conductivity increases as the sintering temperature of the samples decreases, preserving similar values of activation energies in the range 0.95-0.97 eV. According to the space-charge-layer model [38, 40], differences in the specific grain

boundary conductivity are related to different levels of segregation of the trivalent dopant at the space charge layer, which are electrically balanced by the accumulation of oxygen vacancies at the core of the grain boundary.

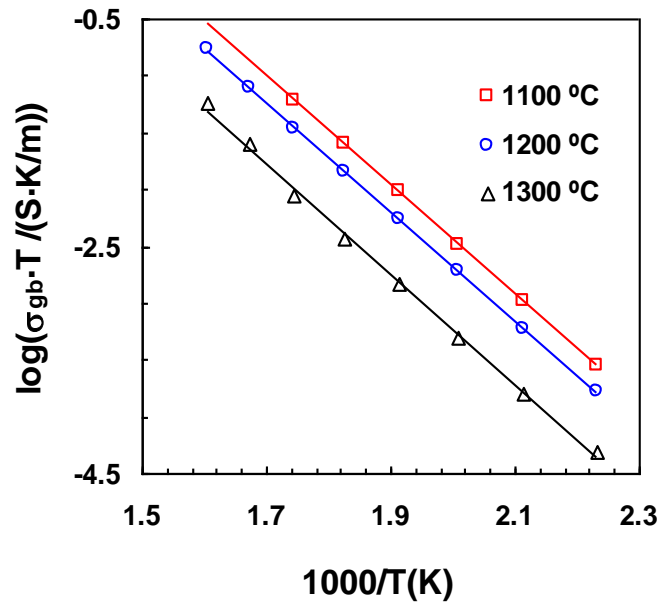


Figure 8. Arrhenius plot of grain-boundary conductivities for $\text{Ce}_{0.9}\text{Gd}_{0.1}\text{O}_{2-\delta}$ sample sintered at different temperatures

As a consequence, a depletion of oxygen vacancies at the space charge layer takes place, with the corresponding appearance of an electrostatic potential in relation to the bulk ($\Delta\phi(x)$), due to differences in the concentration of mobile species, as follows:

$$\frac{[V_{\text{O}}^{\bullet\bullet}]_x}{[V_{\text{O}}^{\bullet\bullet}]_B} = \exp\left(-\frac{2e\Delta\phi(x)}{k_B T}\right) \quad (5)$$

where $[V_{\text{O}}^{\bullet\bullet}]_x$ represents the oxygen vacancy concentration at a generic position x of the space charge layer, $[V_{\text{O}}^{\bullet\bullet}]_B$ is the oxygen vacancy concentration at the bulk and e , k_B and T have their usual meanings. The electrostatic potential is usually determined by solving the Poisson equation under the assumption that the charge density at the space charge layer is mainly established by the dopant segregation, characterized by a constant concentration profile along the space charge layer, as a first approximation (Mott-Schottky model) [38, 40]. Under these conditions, the bulk to grain boundary conductivity could be expressed as:

$$\frac{\sigma_B}{\sigma_{gb}} \approx \frac{\exp(2e\Delta\phi_0 / (k_B T))}{4e\Delta\phi_0 / (k_B T)} \quad (6)$$

where $\Delta\phi_{0\Box}$ represents the space-charge potential at the interface core/space-charge layer. **Figure 9** shows a clear increase of the bulk to grain boundary conductivity ratio as the sintering temperature of the samples increases.

These experimental results are introduced in Eq. 6 for determination of the space charge potential at the interface core/space charge layer (**Figure 10**). As an interesting feature, it is clearly observed an increase of the height of the potential barrier as the sintering temperature increases, thus harming the oxide-ionic transport across the grain boundaries. This is consistent with a higher segregation of trivalent dopant, as the depletion of charge carrier concentration in the space charge layer in relation to the bulk is proportional to the height of the potential barrier [35, 41]

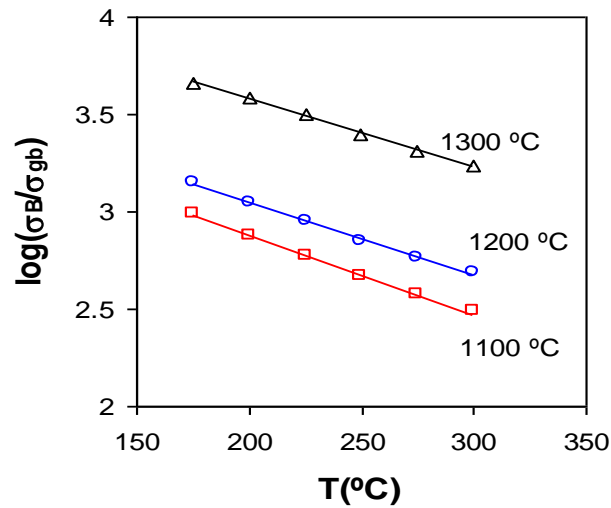


Figure 9. Bulk to grain boundary conductivity ratio as a function of measuring temperature for samples sintered at 1100, 1200 and 1300 °C.

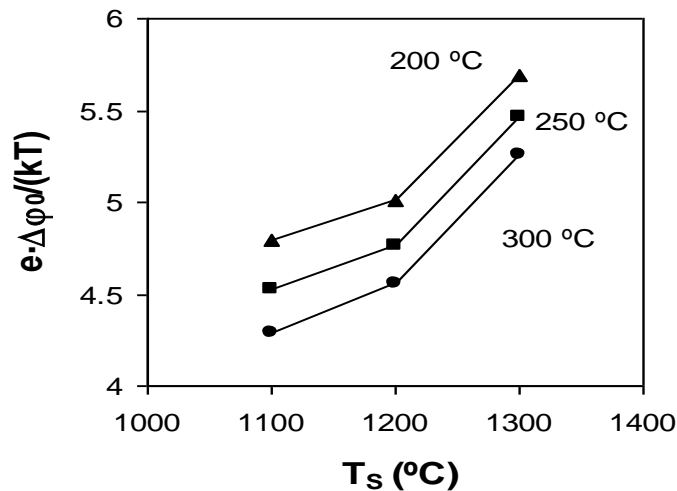


Figure 10. Dimensionless space-charge-potential barrier as a function of sintering temperature obtained using a Mott-Schottky model.

Conclusions

Nanopowder of Ce_{0.9}Gd_{0.1}O_{2-δ} material with the fluorite structure was prepared by a hydrothermal process at low temperature (140 °C). The small particle size of the compound allows to obtain dense ceramic pellets at a sintering temperature as low as 1100 °C. As the sintering temperature was increased, the specific grain boundary conductivity was harmed, affecting the overall transport in the low temperature regime. The space charge layer model was used to analyze the transport properties at grain boundaries. The model suggested that the decrease of the specific grain boundary conductivity was attributable to an increase of the space charge potential barrier, as the segregation of trivalent dopant is expected to increase for higher sintering temperature.

References

1. Yamamoto, O., *Electrochim. Acta.*, 45 (2000) 2423
2. Steele, B.C.H., *J. Mater. Sci.*, 36 (2001) 1053
3. Kharton, V.V., Viskup, A.P., Marozau, I.P., Naumovich, E.N., *Mater. Lett.*, 57 (2003) 3017

4. Minh, N.Q., Takahachi, T., *Science and Technology of Ceramic Fuel Cells*, (Elsevier, Amsterdam, 1995)
5. Singhal, S.C., Kendall, K., *High Temperature Solid Oxide Fuel Cell*, (Elsevier, Oxford, 2004)
6. Boudghene Stambouli, A., Traversa, E., *Renewable Sustainable Energy Rev.*, 6 (2002) 433
7. Wachsman, E.D., Lee, K.T., *Science* 334 (2011) 935
8. Chung, D.Y., Lee, E.H., *J. Alloys Compd.* 374 (2004) 69
9. Fu, Y.P., Lin, C.H., *J. Alloys Compd.* 389 (2005) 165
10. Van herle, J., Horita, T., Kawada, T., Sakai, N., Yokokawa, H., Dokiya, M., *Solid State Ionics*, 86 (1996) 1255
11. Steele, B.C.H., *Solid State Ionics*, 129 (2000) 95
12. Blumenthal, R.N., Hofmaier, R.L., *J. Electrochem. Soc.*, 121 (1974) 126
13. Sims, J.R., Blumenthal, R.N., *High Temp. Sci.*, 8 (1976) 99
14. Tuller, H.L., Nowick, A.S., *J. Electrochem. Soc.*, 126 (1979) 209
15. Chang, E.K., Blumenthal, R.N., *J. Solid State Chem.*, 72 (1988) 330
16. Inaba, H., Tagawa, H., *Solid State Ionics*, 1 (1996) 83
17. Wincewicz, K.C., Cooper, J.S., *J. Power Sources*, 140 (2005) 280
18. Mogensen, M., Sammes, N. M., Tompsett, G. A., *Solid State Ionics*, 129 (2000) 63
19. Minervini, L., Zacate, M.O., Grimes, R.W., *Solid State Ionics*, 116 (1999) 339
20. Steele, B.C.H., *High Conductivity Solid Ionic Conductors*, (Takahashi, T., World Scientific, Singapore, 1989)
21. Sin, A., Dubitsky, Y., Zaopo, A., Arico, S.A., Gullo, L., La Rosa, D., Siracusano, S., Antonucci, V., Oliva, C., Ballabio, O., *Solid State Ionics*, 175 (2004) 361
22. Cheng, J.G., Zha, S.W., Huang, J., Liu, X.Q., Meng, G.Y., *Mater. Chem. Phys.*, 78 (2003) 791
23. Rambabu, B., Ghosh, S., Jena, H., *J. Mater. Sci.*, 41 (2006) 7530
24. Sammes, N.M., Cai, Z., *Solid State Ionics*, 100 (1997) 39
25. Huang, W., Shuk, P., Greenblatt, M., *Solid State Ionics*, 100 (1997) 23
26. Rodriguez-Carvajal, J., Roisnel, T., FullProf.98 and WinPLOTR: New Windows 95/NT Applications for Diffraction, Newsletter, 20 (1998).
27. ZPlot and Zview, A Software Program for IES Measurements and Analysis, (Scribner Associates, NC, USA, 2002)
28. West, R., in *Solid State Chemistry and its Applications*, Wiley, Chichester, (1984) 173.
29. Christie, G.M., Van Berkel, F.P.F., *Solid State Ionics*, 83 (1996) 17
30. Pérez-Coll, D., Sánchez-López, E., Mather, G.C., *Solid State Ionics* 181 (2010) 1033
31. Sánchez-Bautista, C., Dos santos-García, A.J., Peña-Martínez, J., Canales-Vázquez, J., *Solid State Ionics* 181 (2010) 1665
32. Faber, J., Geoffroy, G., Roux, A., Abélard, P., *Appl. Phys. A*, 49 (1989) 225
33. Wang, D.Y., Park, D.S., Griffith, J., Nowick, A.S., *Solid State Ionics* 2 (1981) 95
34. Kilner, J.A., *Solid State Ionics* 129 (2000) 13
35. Pérez-Coll, D., Núñez, P., Frade, J.R., *J. Electrochem. Soc.*, 153 (3) (2006) A478
36. Huang, K., Feng, M., Goodenough, J.B., *J. Am. Ceram. Soc.*, 81 (1998) 357
37. Abrantes, J.C.C., Labrincha, J.A., Frade, J.R., *J. Eur. Ceram. Soc.*, 20 (2000) 1603
38. Guo, X., Waser, R., *Prog. Mater. Sci.*, 51 (2006) 151
39. Ferreira, A.A.L., Horovistiz, A.L., Abrantes, J.C.C., Pérez-Coll, D., Núñez, P., Frade, J.R., *Mater. Res. Bull.* 44 (2009) 884
40. Guo, X., Maier, J., *J. Electrochem. Soc.*, 148 (3) (2001) E121
41. Guo, X., Sigle, W., Maier, J., *J. Am. Ceram. Soc.* 86 (1) (2003) 77

(2016) ; <http://www.jmaterenvirosci.com/>